Improving damage resistance of solid-state battery cathodes with block copolymers: A non-linear diffusion-mechanics study at the microscale

Soheil Bazazzadeh [a,1], Mauro Pasta [b,1], Łukasz Figiel [a,c,1,*]

[a] *IINM, WMG, University of Warwick, CV4 7AL, UK*
[b] *Department of Materials, University of Oxford, Parks Road, Oxford OX1 3PH, UK*
[c] *Warwick Centre for Predictive Modelling (WCPM), University of Warwick, CV4 7AL, UK*

ARTICLE INFO

ABSTRACT

Minimizing interfacial failure in the composite cathode remains a crucial challenge to unravel the full potential of all solid-state batteries (ASSBs). Polymer-based ASSBs offer promising means of minimizing those damage effects due to their high ductility. However, multicomponent polymers such as block copolymers (BCPs) are needed to meet requirements for both ionic conductivity and mechanical resistance. This study aims to provide a new insight into the combined effects of block copolymer composition (soft-to-hard phase ratio) and interfacial strength on the coupled diffusion-mechanics response of an ASSB cathode, achieved by proposing a non-linear computational micromechanics approach. The approach combines a pressure-dependent diffusion process, interfacial gap-dependent diffusivity, and advanced elasto-viscoplastic constitutive model for a BCP, and it is implemented numerically within a non-linear finite element framework. Two cathode design concepts are explored here, with and without the BCP coating. Results from these case studies suggest that there is a strong interplay between the interface strength (between active particles and the BCP matrix), the BCP material composition, and the interfacial diffusivity. It is found that interfacial damage can be minimized by increasing both the interfacial strength and the amount of the soft component in the BCP system. If the diffusivity across the interface is damage-dependent, the latter is reduced when the BCP is predominantly made of the hard phase. Ultimately, a simple sensitivity analysis reveals that interfacial strength plays a vital role in minimizing interfacial damage, while the coating thickness is the least influential design parameter.

1. Introduction

Over the last few years, ASSBs lithium metal batteries have been widely investigated as an alternative to state-of-the art Li-ion batteries, due to their high specific energy storage and densities, long cycling lifespans, low-discharge rates, and increased safety [1–5]. However, due to their solid-state nature, the ASSBs are more prone to mechanical degradation than their aqueous electrolyte-based battery counterparts. In fact, deformations arising from the volumetric expansion of the cathode active material, and externally applied pressure cannot be easily accommodated within geometrical constraints of ASSBs. As a result, mechanical failure can occur within the bulk and at various interfaces (e.g. active material/electrolyte interface) in the form of voids and cracks that may disrupt both the electrochemical performance and structural integrity of the battery [6–9]. These effects are of particular importance to ASSBs with rigid/brittle components such as ceramic electrolytes that may suffer from cracks, delaminations or debondings during battery operation [4–9].

Therefore, there has been an increasing interest in using alternative materials and design concepts for ASSBs to minimize those damage phenomena. They include applying more ductile solid electrolyte components such as polymers. Although solid-state polymer electrolytes offer excellent processability light weight, and good resistance to fracture, they suffer from low ionic conductivity (especially at lower temperatures) [4]. To address that challenge researchers have looked into developing polymer–ceramic composite electrolytes that combine benefits of both material systems [10,11]. Another viable route is to develop future damage-resistant materials for ASSBs in the form of (di-)block copolymers (BCPs) where one component provides sufficient mechanical resilience while the other controls the ionic conductivity [12,13]. Such a multicomponent material approach can offer promising means to mitigate effects of volumetric changes, especially when combined with relevant battery design concepts including polymer-based coating of active materials [14,15].

---

* Correspondence to: WMG, University of Warwick, Coventry, CV4 7AL, UK.
E-mail address: l.w.figiel@warwick.ac.uk (Ł. Figiel).

[1] All authors contributed equally to the revision.

However, the main challenges related to the full exploitation of BCPs in ASSBs are related to their large design parameter space that ultimately requires better understanding of the relationship between their morphology and performance within ASSBs. Hence, a systematic study of those relations is of key importance to provide some design principles of those materials for ASSBs. Clearly, a systematic experimental investigation of those relationships poses the well-known challenges i.e. resources and time required. The advanced materials modelling can offer a significant assistance and therefore can help to provide new insights into the damage behaviour of ASSBs using BCP materials.

In comparison with more traditional Li-ion batteries where a significant amount of research on damage was carried out (see for example [16–18]), modelling of ASSBs, and in particular of their damage behaviour, has attracted less attention. Among such models, it is worthwhile highlighting some examples of models (both analytical and computational) attempting to provide insights into damage behaviour at interfaces around active particles and solid electrolytes at the microscale [19–23]. In particular, a one-dimensional (1D) analytical linear elastic model was proposed in [19] to capture the interfacial mechanical damage between an active particle and solid electrolyte. In [20], a gradient enhanced damage model was developed to predict damage during Li-ion battery cycling based on particle size and spacing. Moreover, a phase-field electro-chemo-mechanical model approach was recently proposed in [21] to predict the void evolution at the Li-electrolyte interface in ASSBs. Electro-chemo-mechanical approaches were proposed at the macroscopic and microscopic ASSB levels under the assumption of linear elasticity [22–24]. The majority of those works have focussed on inorganic and rigid electrolytes, modelled as linear elastic solids. However, to investigate accurately the effects of polymeric components on the mechanical response of the ASSB, their non-linear and time-dependent nature must be captured by a relevant elasto-viscoplastic constitutive model. Furthermore, in the context of BCPs, the relationship between their material composition (e.g. component ratio) and macroscopic mechanical response must be additionally accounted for within their constitutive model to fully unveil their effects on the mechanical response of a polymer-based ASSB.

The aim of this work is to provide a new insight into the use of BCPs in ASSB cathodes (either as matrices or coatings) by exploring a complex interplay between their non-linear response, interfacial damage and Li-ion transport at the microscale of a model cathode. This is achieved by developing a 3D non-linear computational diffusion-mechanics approach that significantly extends our earlier work [25]. The main contribution here is related to the description of the non-linear constitutive response of a BCP by adopting the concept of the composite inclusion [26] to incorporate morphological features of a model di-block copolymer such as soft-to-hard component ratio. The modelling approach is then applied to two design case studies for a BCP-based cathode to study the effects of the soft-to-hard component ratio, interfacial strength and interfacial diffusivity on the magnitude of the interfacial damage, and their implications on the Li mass transport. The proposed approach is complemented with a simple sensitivity analysis to reveal the most crucial cathode design parameters that affect interfacial damage in ASSBs.

The paper starts with the detailed description of two design case studies and related modelling assumptions. It is then followed by the formulation of the diffusion-mechanics problem that contains a detailed description of the BCP constitutive model in terms of the composite inclusion concept. Standard tensor notation is employed here to describe the details of the model. Results of the simulations for two design case studies are complemented by a simple gradient-based sensitivity analysis of the model design parameters.

2. Background and main assumptions

A typical ASSB is made of a positive electrode (cathode), and a negative electrode (anode), separated by a solid-state electrolyte (SE), and current collectors (CC) attached to the external sides of both electrodes (see Fig. 1(a)).

Active particles (AP) reside in the cathode layer made of a material depending on the design concept adopted here (see below). During charge/discharge (lithiation/delithiation) cycles, the volume of the APs change cyclically and can lead to the debonding and the subsequent disruption of ionic conductivity upon formation of an interfacial gap. Hence, the battery material design should aim at minimizing the interfacial gap (or ideally avoiding it at all) by a careful combination of the matrix material surrounding the particles, and also the adhesion of the AP/matrix interface.

Two conceptual material configurations for a ASSB battery, which for brevity are called *Designs*, are studied in the context of the use of BCP material system. In particular, *Design I* (Fig. 1(b)) exploits the use of BCP as the matrix material spanning the battery across from the current collector right to the anode — hence, the cathode particles are assumed to be embedded within the BCP matrix, which is assumed here to be seamlessly connected with the solid electrolyte layer. From the manufacturing point this design may be achieved via an extrusion process traditionally used for thermoplastic polymers – then, the extruded layers of the solid electrolyte and cathode particle-reinforced BCP layer can be thermally bonded under pressure taking advantage of the same kind of polymer – the latter can also help to achieve a good connection at the interface between the solid electrolyte and cathode layers. 3D printing processes can also be considered to achieve this design. The *Design I* concept has the advantage of avoiding an imperfect interface between the cathode and solid electrolyte (especially in the case of ceramics-based solid electrolyte).

For the *Design II* concept (Fig. 1(c)), the APs in the cathode are coated by a BCP layer of a certain finite thickness. The coated particles are then assumed to be embedded in a ceramic matrix of the cathode layer that is adjacent to the ceramic solid electrolyte layer. The main advantage of this design is expected to result from a deformable BCP coating that can minimize the effects of volumetric expansion of APs. In both cases, the focus here is on the interface between APs and BCP matrix (*Design I*), and APs and BCP coating (*Design II*).

For computational convenience a highly complex cathode microstructure consisting of irregularly shaped NMC APs (see e.g. [27–29]) is idealized with a regular arrangement of spherical particles within the cathode. Moreover, it is assumed that the negative electrode is made of a monolithic Li-metal that is a promising material candidate for the anode [30,31]. Hence, as the focus here is on exploring interfacial damage processes occurring in the cathode, and that it is relatively stiff (mechanically) compared to our material components (especially BCP), it has been replaced by relevant mechanical constraints (see Section 3.3).

3. Formulation of the problem

3.1. Governing equations for the bulk components

Electrochemical processes occurring in ASSBs during their cycling lead to transport of ions and electrons, and deformations within a typical ASSB cathode. Here, we neglect electrical fields, and focus specifically on the coupling between diffusion of Li-ions and mechanical stresses. In particular, Li-ion concentration-driven volumetric changes (expansion and contraction) of APs lead to mechanical stresses due to various geometrical constraints within the battery. In turn, stresses can affect Li-ion transport through the constitutive equation (i.e. pressure-dependent diffusion flux) and interfacial damage (i.e. gap-dependent interfacial diffusivity) — both will be discussed in subsequent sections.
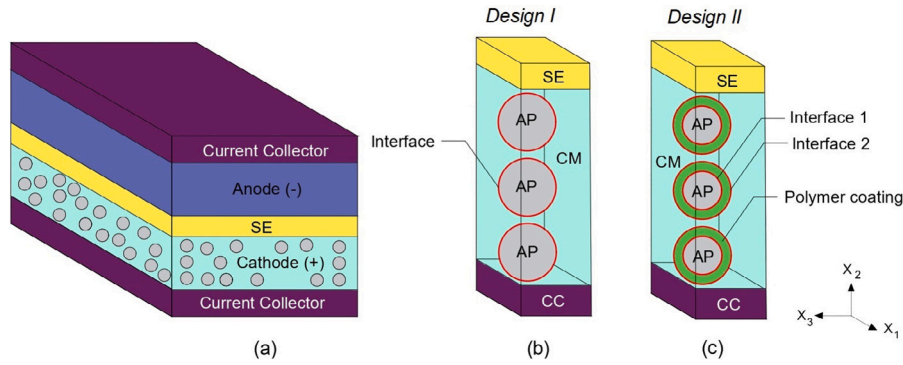
S. Bazazzadeh et al.

Fig. 1. Schematic representation of a typical layered ASSB — overall view; and two proposed *Designs I* and *II*.

The stress- and mass-balance equations are used here as two governing equations that need to be satisfied within each battery component, as follows:

$$\nabla \cdot \boldsymbol{\sigma} = 0 \tag{1}$$

$$\frac{\partial c}{\partial t} = -\nabla \cdot \mathbf{j} \tag{2}$$

where $\boldsymbol{\sigma}$ is the Cauchy stress tensor, $\mathbf{j}$ stands for the mass flux and c indicates the Li molar concentration.

Eqs. (1)–(2) are complemented in the usual way by relevant constitutive laws that govern the material response, AP/BCP interface conditions (traction–separation law; interfacial diffusivity), and boundary conditions.

3.1.1. Elasto-viscoplastic constitutive model for a block copolymer (BCP) matrix

The mechanical response of a typical thermoplastic polymer is complex, and in general it is time- and temperature-dependent, and should be described with an elasto-viscoplastic constitutive model in the finite-strain framework. An additional complexity related to a thermoplastic BCP arises from its complex morphology that should also be reflected in the constitutive model. Here it is assumed that the BCP morphology consists of two phases, hard (H) and soft (S), which results in lamellar building blocks ('grains' or 'inclusions') where each of them has a certain orientation (see Fig. 2(a)) — however, ultimately they are all assumed to be randomly oriented giving rise to the initially isotropic mechanical response. Each 'grain' is approximated here as a two-layer unit cell known as the composite inclusion (see Fig. 2(b)).

It is noteworthy to mention that the lamellar morphology is only a convenient approximation here to a range of possible morphologies BCPs can take on, depending on a range of variables including soft-to-hard phase ratio, f_0^S, or thermodynamic compatibility between phases. For example, BCP morphologies can vary from a 'body centre cubic' (BCC) to the 'inverted' BCC morphology, where the lamellar morphology typically occurs for f_0^S between 0.38 and 0.6 [32].

The composite inclusion model [26] is adopted here to predict the mechanical response of the BCP with a morphology composed of lamellae-like inclusions of different orientations.

3.1.2. Composite inclusion model for the BCP

The original composite inclusion model (CIM) has been developed to capture the elasto-viscoplastic behaviour of semi-crystalline polymers [26]. The response of those systems was represented through an aggregate of two-phase inclusions consisting of anisotropic crystalline and amorphous phases. Here, we adopt the CIM to capture an aggregate composed of two different elasto-viscoplastic phases where both are assumed to be amorphous. Hence, each composite inclusion consists of a 'hard' (H) and 'soft' (S) elasto-viscoplastic layer which are mechanically coupled with each other (see Fig. 2(b)). As finite deformations

are considered here, the current volume fraction (i.e. in the deformed configuration) of the respective phase α depends on the initial volume fraction f_0^α:

$$f^\alpha = \frac{f_0^\alpha J^\alpha}{f_0^S J^S + (1-f_0^S)J^H}; \quad \alpha = S, H \tag{3}$$

where $J^\alpha = \det(\mathbf{F}^\alpha)$ stands for the volume ratio of each phase, and $\mathbf{F}^\alpha$ denotes the total deformation gradient (second-order tensor) of each phase.

The inclusion-averaged deformation gradient, $\mathbf{F}^I$, and the inclusion-averaged Cauchy stress (second-order tensor), $\boldsymbol{\sigma}^I$, are calculated by the volume-weighted average of the deformation gradient of soft and hard phases as:

$$\mathbf{F}^I = f_0^S \mathbf{F}^S + (1-f_0^S)\mathbf{F}^H \tag{4}$$

$$\boldsymbol{\sigma}^I = f^S \boldsymbol{\sigma}^S + (1-f^S)\boldsymbol{\sigma}^H \tag{5}$$

The kinematical coupling between the hard and soft phases is maintained by enforcing compatibility on the deformation gradients:

$$\mathbf{F}^S \cdot \mathbf{x}_0^I = \mathbf{F}^H \cdot \mathbf{x}_0^I = \mathbf{F}^I \cdot \mathbf{x}_0^I \tag{6}$$

where $\mathbf{x}_0^I$ stands for an arbitrary vector in the plane of the interface. Furthermore, the following continuity of tractions at the interface is assumed as:

$$\boldsymbol{\sigma}^S \cdot \mathbf{n}^I = \boldsymbol{\sigma}^H \cdot \mathbf{n}^I = \boldsymbol{\sigma}^I \cdot \mathbf{n}^I \tag{7}$$

where, $\mathbf{n}^I$ is the unit normal to the interface in the current configuration.

A local–global interaction law must be formulated in order to relate the volume-averaged deformation of each composite inclusion to the overall deformation applied to an aggregate of inclusions. For this we employ the Taylor's interaction model used in polycrystal plasticity [33, 34]. In this model, we assume that the inclusion-averaged deformation gradient for each composite inclusion is equal to the total applied deformation gradient of the entire aggregate:

$$\mathbf{F}_i^I = \bar{\mathbf{F}} \tag{8}$$

From Eqs. (6)–(8), one can construct the following systems of equations for each inclusion in the system as:

$$\begin{cases} \mathbf{F}^S \cdot \mathbf{x}_0^I = \mathbf{F}^H \cdot \mathbf{x}_0^I = \mathbf{F}^I \cdot \mathbf{x}_0^I \\ \boldsymbol{\sigma}^S \cdot \mathbf{n}^I = \boldsymbol{\sigma}^H \cdot \mathbf{n}^I = \boldsymbol{\sigma}^I \cdot \mathbf{n}^I \\ \mathbf{F}_i^I = \bar{\mathbf{F}} \end{cases} \tag{9}$$

By solving Eq. (9), one is able to find the deformation gradient in each phase, $\mathbf{F}^\alpha$. Then, one can compute the Cauchy stress $\boldsymbol{\sigma}^\alpha$ in each phase of the inclusion via constitutive relations introduced below. Accordingly, the total stress field in each inclusion is obtained by
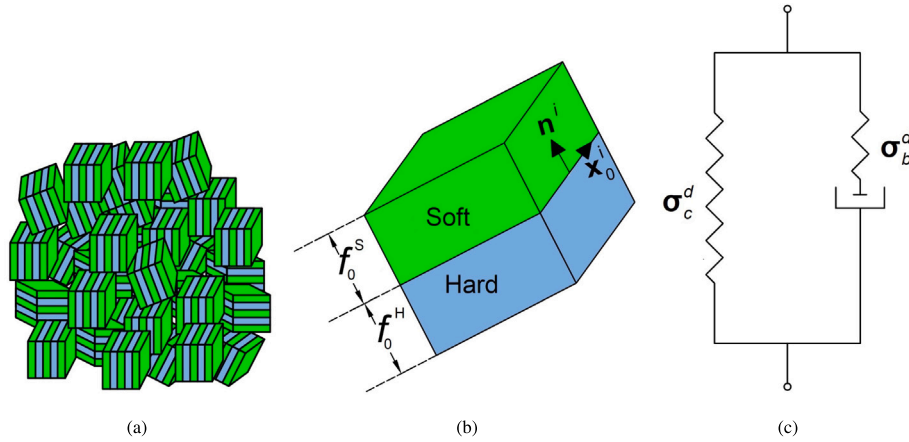
Fig. 2. Constitutive model of a block copolymer (BCP): (a) Lamellar morphology as an aggregate of randomly oriented composite inclusions (b) two-phase composite inclusion (c) 1D rheological representation of an elasto-viscoplastic behaviour of each phase α in the BCP.

Eq. (5) and the total Cauchy stress tensor of the aggregate $\bar{\sigma}$ can be calculated by the global volume-averaging as:

$$\sum_{i=1}^{N} f_i^{\mathrm{I}} \, \sigma_i^{\mathrm{I}} = \bar{\sigma} \tag{10}$$

in which, N stands for the total number of inclusions. According to the Taylor's assumption, the current volume fraction of each inclusion f_i^{I} remains constant and it is equal to its initial value as:

$$f_i^{\mathrm{I}} = f_{0_i}^{\mathrm{I}} = \frac{1}{N} \tag{11}$$

The composite inclusion model requires the definition of constitutive models governing the mechanical response of each (soft, hard) elasto-viscoplastic phase. Here we exploit a two-process elasto-viscoplastic model for each where polymer resistance to deformation results from two sources: (1) inter-atomic bond potentials that can relax through diffusive molecular motions and (2) conformational entropy. A 1D representation of the model is shown in Fig. 2(c). Hence, the total Cauchy stress is split into its deviatoric and volumetric parts in each component of the composite inclusion (soft/hard), and it is given by:

$$\sigma^{\alpha} = \sigma^d + \sigma_v = \sigma_b^d + \sigma_c^d + \sigma_v, \quad \alpha = \mathrm{H, S} \tag{12}$$

where, σ_b^d and σ_c^d are the bond-stretching and conformational components of the deviatoric part of Cauchy stress [35] as depicted in Fig. 2(c); and σ_v stands for the volumetric stress tensor which assumes purely elastic volumetric response. Following [36,37], relevant stress components in Eq. (12) are given by:

$$\sigma_b^d = G_b \, J_e^{-1} \, \bar{\mathbf{B}}_e^d \tag{13}$$

$$\sigma_c^d = G_c \, J_e^{-1} \, \bar{\mathbf{B}}^d \tag{14}$$

$$\sigma_v = K \, (1 - J_e^{-1}) \, \mathbf{I} \tag{15}$$

where, G_b, G_c, K and $\mathbf{I}$ are the shear, strain hardening, bulk moduli, and the second-order identity tensor respectively. Furthermore, $\bar{\mathbf{B}}_e^d$ and $\bar{\mathbf{B}}^d$ are the isochoric elastic and total left Cauchy–Green tensor given by:

$$\bar{\mathbf{B}}_e^d = (J_e)^{-\frac{2}{3}} \mathbf{F}_e \cdot \mathbf{F}_e^T \tag{16}$$

$$\bar{\mathbf{B}}^d = (J)^{-\frac{2}{3}} \mathbf{F} \cdot \mathbf{F}^T \tag{17}$$

where, $\mathbf{F}$ and $\mathbf{F}_e$ stand for the total and elastic deformation gradient tensors, respectively; $J = \det(\mathbf{F})$ and $J_e = \det(\mathbf{F}_e)$ represent the total and elastic volume ratios, respectively.

Note that in order to account for viscoplastic deformations, the total deformation gradient $\mathbf{F}$ in Eq. (17), can be multiplicatively decomposed into the elastic $\mathbf{F}_e$ and plastic $\mathbf{F}_p$ deformation gradients as:

$$\mathbf{F} = \mathbf{F}_e \cdot \mathbf{F}_p \tag{18}$$

Moreover, the rate dependence of non-linear deformations is described by the plastic part of the deformation rate tensor as:

$$D_p = \frac{\sigma_b^d}{2\eta} \tag{19}$$

where, η represents the viscosity given by Eyring's relationship [37]:

$$\eta = A \, \tau_0 \, \frac{(\tau_{eq}/\tau_0)}{\sinh{(\tau_{eq}/\tau_0)}} \tag{20}$$

where, A and τ_0 are Eyrings's material parameters, respectively. In Eq. (20), τ_{eq} is the equivalent deviatoric stress and it is defined as:

$$\tau_{eq} = \sqrt{\frac{1}{2}\mathrm{tr}(\sigma_b^d \cdot \sigma_b^d)} \tag{21}$$

Note that the plastic deformation is assumed to be isochoric and $\det(\mathbf{F}_p) = 1$, and above equations are given under the assumption of plastic spin-free deformations, i.e. $\mathbf{W}_p = \mathbf{0}$ (and thus $J = J_e$).

3.1.3. Mechanical behaviour of other bulk components in the battery

Here it is assumed that the mechanical response of active particles (APs) and the current collector (CC) is linear elastic, isotropic and time-independent. The SE layer is assumed to follow a linear elastic behaviour to represent a typical ceramic SE in *Design II*, while its behaviour is assumed to be elasto-viscoplastic (BCP) in *Design I*.

3.1.4. Constitutive law for Li-ion transport (diffusion)

Pressure-dependent Fick's 1st law [38] is used here to model the transport of Li-ions in active particles (APs), and it is given by:

$$\mathbf{j} = -D \, \nabla c + \frac{3 \, \beta^{iso} D}{RT} c \nabla \sigma_h \tag{22}$$

where, D, R and T are the diffusion constant, universal gas constant and temperature, respectively; β^{iso} denotes the chemical expansion coefficient in the chemo-mechanical coupling via the Vegard's law (see below Section 3.2); $\nabla \sigma_h$ is the gradient of the hydrostatic pressure that arises in active particles (APs) of the cathode.

For completeness, it must be mentioned that the diffusion law applied to the other battery components (i.e. solid electrolyte, cathode matrix and coating, and current collector) is assumed to be pressure-independent. This is due to the fact that the deformation caused by lithiation/delithiation in the active particles (APs) is higher compared to these components, resulting in smaller stresses and negligible pressure-dependent effects on their diffusion behaviour.
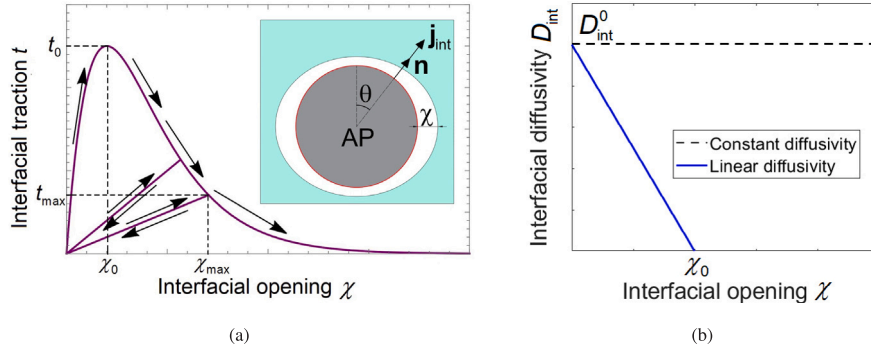
Fig. 3. Constitutive representation of AP/BCP matrix (or AP/BCP coating) interface: (a) mechanical response — traction–separation law with loading–unloading paths; (b) interfacial diffusivity — gap-independent (constant) and gap-dependent (linear) diffusivity.

3.2. Constitutive representation of interfaces

Two interfaces are present in the model: (1) AP/BCP matrix (Design I) or AP/BCP coating (Design II), and (2) cathode/current collector. The latter is assumed to have an infinite strength (so called 'perfect' mechanical bonding) and thus no damage is considered for that interface in this work. As a result, the diffusivity across the interface (2) is not affected by any interfacial damage. Both mechanical and non-mechanical response of the interface (1) is described in the two subsequent subsections.

3.2.1. Mechanical response of the AP/BCP matrix (or AP/BCP coating) interface

The mechanical response at the interface is assumed to be governed by the traction–separation (T–S) law relating the interfacial opening displacement χ to the traction t via the universal binding law [39] given by:

$$t = t_0 \frac{\chi}{\chi_0} \exp\left(1 - \frac{\chi}{\chi_0}\right) \tag{23}$$

where t_0 stands for the interface strength and χ_0 corresponds to the gap at damage initiation (see Fig. 3(a)). Moreover, a linear unloading to the origin is assumed to follow:

$$t = \frac{t_{\max}}{\chi_{\max}} \chi \tag{24}$$

where $\chi_{\max}$ denotes the maximum opening that has been achieved during previous loading and $t_{\max}$ is the corresponding cohesive traction.

It must be mentioned that a linear traction–separation law is assumed for (uncoupled) shear modes 2 and 3, where no damage occurs. Additionally, the stiffness of the shear modes was assumed as $k_s = 0.5$ MPa/μm.

3.2.2. Diffusion across AP/BCP matrix (or AP/BCP coating) interface

Using the classical concept of the overpotential, a simplified phenomenological Li transport model across the interface (from/into the APs) [25], is used here as:

$$\mathbf{j}_{\mathrm{int}} \cdot \mathbf{n} = D_{\mathrm{int}}(c_{\mathrm{int}}^{\mathrm{AP}} - c_{\mathrm{ref}}^{\mathrm{AP}}) \, c_{\mathrm{int}}^{\mathrm{M}} \tag{25}$$

where $\mathbf{j}_{\mathrm{int}}$, $\mathbf{n}$ and D_{int} stand for the Li flux at the interface, outward normal vector in the deformed configuration and interfacial diffusivity, respectively (see Fig. 3(a)). Moreover, $c_{\mathrm{int}}^{\mathrm{AP}}$ and $c_{\mathrm{int}}^{\mathrm{M}}$ stand for the Li concentration at the interface on the AP and BCP matrix sides, respectively; $c_{\mathrm{ref}}^{\mathrm{AP}}$ is related to the ultimate desired Li concentration at the end of the charge/discharge process, and it is set as $c_{\mathrm{ref}}^{\mathrm{AP}} = c_{100\%}^{\mathrm{AP}}$ and $c_{\mathrm{ref}}^{\mathrm{AP}} = c_{0\%}^{\mathrm{AP}}$ for the maximum charge and discharge processes, respectively. Note that in this study, it is assumed that the battery is initially discharged and $c_{0\%}^{\mathrm{AP}} = c_{\max}^{\mathrm{AP}}$. In turn, some residual Li concentration $c_{\mathrm{res}}^{\mathrm{M}}$ is assumed to remain in the matrix [25,27].

3.2.3. Coupling between diffusion and mechanics

Coupling between diffusion and mechanics occurs in APs, and it is related to three mechanisms. The first one is based on the Vegard's law introduced in [16], given by:

$$\varepsilon_{\mathrm{Li}} = (c_{0\%}^{\mathrm{AP}} - c^{\mathrm{AP}}) \zeta \tag{26}$$

Eq. (26), accounts for the delithiation/lithiation induced by the Li concentration in the active particles at a given time, c^{AP}. ζ stands for the volume change tensor where $\zeta_{ij} \neq 0$ if $i = j$ and $\zeta_{ij} = 0$ if $i \neq j$. In this paper, APs are assumed to be isotropic, i.e. $\zeta_{11} = \zeta_{22} = \zeta_{33} = \beta^{iso}$ (see Eq. (22)).

The second mechanism is the effect of hydrostatic pressure gradient, $\nabla \sigma_h$, on the mass flux introduced in [38] see Eq. (22).

The third mechanism emerges due to the relation between the mass flux $\mathbf{j}$ across the AP/BCP matrix (AP/BCP coating) interface and interfacial opening χ. This effect is imposed here through the interface diffusivity D_{int} as a function of χ. Due to the lack of experimental evidence two idealized relations between D_{int} and χ are considered here (see Fig. 3(b)): (1) constant interfacial diffusivity corresponding to no interfacial damage on D_{int}, and (2) gap-dependent (linearly decaying) interfacial diffusivity D_{int} with χ until $\chi = \chi_0$ when $D_{\mathrm{int}} = 0$.

3.3. Boundary conditions

The boundary conditions used in subsequent non-linear finite element (FE) simulations are shown in Fig. 4(a). They apply to both Design I and II.

To model transport of Li-ions from/into the cathode or into/from the anode the Li flux is applied to the top surface (i.e. top of the solid electrolyte layer) as follows:

$$\mathbf{j} \cdot \mathbf{n} = D^{\mathrm{SE}} (c^{\mathrm{SE}} - c_{\mathrm{res}}^{\mathrm{SE}}) \tag{27}$$

where $\mathbf{n}$ is the outward normal vector on the top surface in the deformed configuration; D^{SE} and c^{SE} stand for the surface diffusivity and Li-ion concentration at a given time, respectively. During the charge process, the Li-ion transport is from the cathode to the top boundary, and the reverse direction is true for the discharge process. The initial Li-ion concentration c^{SE} corresponding to time $t = 0$ s is set to the residual Li concentration, $c_{\mathrm{res}}^{\mathrm{SE}}$ (see Section 3.2.2) — note that the residual Li-ion concentration is assumed to be constant during the whole charge/discharge process. Moreover, it is assumed that the Li flux takes place only in vertical (x_2) direction and therefore other boundaries are considered to be flux free, i.e. $\mathbf{j} \cdot \mathbf{n} = 0$ (see Fig. 4(a)).

As mentioned above, for computational efficiency Li-metal anode is not modelled here, and it is replaced by relevant constraints. Vertical degrees of freedom (u_2 displacements) are constrained on the top (solid electrolyte (SE)) and bottom (current collector (CC)) surfaces, i.e. $u_2 = 0$. Moreover, one of the corner nodes on the top surface is additionally
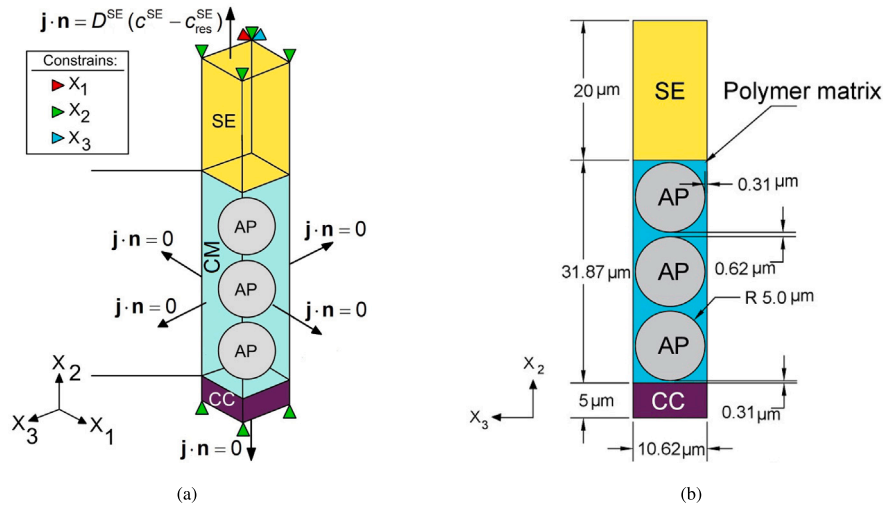
Fig. 4. (a) Geometry and boundary conditions; (b) Microstructure dimensions in $x_2 - x_3$ plane.

constrained in x_1 and x_3 directions, i.e. $u_1 = u_3 = 0$ to avoid any rigid body motion. Mechanical periodic boundary conditions (in terms of displacements) are applied to lateral surfaces of the geometrical model to mimic an in-situ characteristics of the microstructure.

4. Material properties and microstructural characteristics

Polycrystalline Lithium Nickel Manganese Cobalt Oxide ($LiNi_xMn_yCo_zO_2$, $x + y + z = 1$) (NMC) is assumed here as a typical active material/particles in the cathode [40]. Based on the SEM images in [27–29,41], the cathode can consist of nearly spherically shaped NMC particles [27] with an average diameter of 10 µm. The volume fraction of APs in the cathode used in this paper is set to 43.46% — this value is connected with the assumed (idealized) regular (square) packing of spherical APs in the cathode, particle diameter (10 µm), interparticle distances, and cathode thickness. Note that the assumed volume fraction of APs is much lower than the typical one (66.5%) used in ASSB cathode [27], where nearly spherically shaped NMC particles are typically touching each other — that enables larger volume fractions of APs in ASSB cathodes. To account for these effects, the current modelling approach would need to incorporate additional interfacial interactions in terms of contact and friction — however, to treat this efficiently from the computational point of view, particle-based computational approaches such as Discrete Element Method (DEM) [42,43] may be more suitable.

The NMC APs change their volume as a result of cycling with a maximum change of about 5% [27–29]. For simplicity, volumetric changes of NMC APs are assumed to be isotropic. Young's modulus of NMC was measured in the literature by targeted and grid nanoindentation techniques [28]. In this study, an average value of the Young's modulus (E^{AP}) of 130 GPa and Poisson's ratio (ν^{AP}) of 0.25 [44] are used in FE simulations here. Stoichiometric coefficients relating $x_{100\%}$ (100% state of charge at $t = 0$ s) and $x_{0\%}$ (0% state of charge at $t = t_c$) of NMC_{811} are taken from [27] as 0.2567 and 0.9072, respectively. Moreover, considering the maximum Li-ion concentration c_{max}^{AP} as 50,483 [27], one is able to calculate the $c_{100\%}^{AP}$ and $c_{0\%}^{AP}$ as 13 and 45.8 $fmol/m^3$ [25], respectively. Note that the maximum Li-ion concentration is calculated from the theoretical specific capacity of 276.4 mAh/g and density of 4.95 kg/dm^3. Knowing the volume change of the APs (5%) together with the chosen concentrations ($c_{0\%}^{AP}$ and $c_{100\%}^{AP}$), one is able to calculate the coefficient β^{iso} as 0.0004958. In the simulations, the Li diffusion coefficient for the AP (D^{AP}) was selected as 0.025 $\mu m^2/s$, in accordance with the reported range of values found in the literature, which falls between 10^{-14} and 10^{-8} cm^2/s [45,46]. Moreover, the same value for the interface diffusivity is taken as 0.025 $\mu m/s$ (see Table 1). The

block copolymer is assumed to consist of poly(ethylene oxide) (PEO) and polycarbonate (PC) denoted here as a soft and hard BCP material component, respectively. Young's modulus and Poisson's ratio of the PEO are taken from [25] while other model parameters (A, τ_0, G_C) are assumed as presented in Table 1. For the PC component, mechanical and viscosity parameters were adopted from [36], and are summarized in Table 1. The effective value of the Li diffusion coefficient (D^M) for the BCP is assumed to be equal to 3 $\mu m^2/s$. The SE layer in *Design II* is assumed to be a ceramic argyrodite (Li_6PS_5Cl), a popular candidate for ASSBs [47] — its mechanical behaviour is modelled here as linear elastic and isotropic, with the Young's modulus E^C = 22.1 GPa [47] and Poisson's ratio, ν^{AP} = 0.37 [48]. Moreover, the AP coating is made of the same BCP used in *Design I*. Corresponding mechanical and transport properties are in Table 1. The current collector (CC) is assumed to be linear elastic and isotropic, and defined by two elastic constants (see Table 1). The value of Young's modulus assumed here is between the value of aluminium (70 GPa) and stainless steel (190 GPa), two candidate materials for current collectors for cathodes in Li-ion batteries [49]. The current collector is only included here to account for its mechanical effects – no Li-ion transport is modelled through the collector – thus, the diffusion constant is assumed to be 0 $\mu m^2/s$ (see Table 1). Moreover, the diffusivity coefficient for the SE is assumed to be 3 $\mu m^2/s$, while the residual Li-ion concentration is assumed to be 43 $fmol/\mu m^3$.

Furthermore, the corresponding dimensions of the cathode microstructure are shown in Fig. 4(b).

5. Numerical implementation of the model

Implementation of the model was carried out with user-defined subroutines in ABAQUS. Due to the similarities between the diffusion and heat transfer equations, coupling of the mass diffusion and mechanics is carried out via a fully-coupled thermo-mechanical analysis capability of ABAQUS. To include the effect of the hydrostatic pressure on the Fick's law defined by Eq. (22) in Section 3.1.4, a user-defined subroutine UMATHT was used. The composite inclusion constitutive model (Taylor's assumption) for the block copolymer (see Section 3.1.2) was implemented using a UMAT subroutine. Moreover, the gradient of the hydrostatic pressure needed in the UMATHT subroutine was passed from the UMAT subroutine using a UEXTERNALDB user subroutine as depicted in Fig. 5. Additionally, the equations governing the interfacial behaviour between APs and BCP (see Section 3.2) are implemented using a UINTER user subroutine and through surface-to-surface contact ("master"/"slave" approach) [25]. Mechanical periodic conditions are incorporated as linear multiple constrains via the command *Equation. The entire solution procedure with ABAQUS is summarized as a flowchart in Fig. 5.
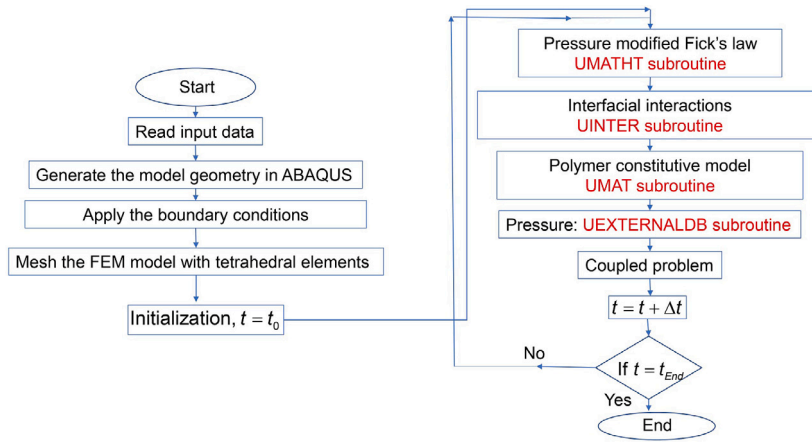
Fig. 5. Flowchart of the non-linear finite element solution procedure with relevant user subroutines for ABAQUS.

Table 1
Parameter set for the simulations.

Symbol	Description	Value	Reference
d^{AP}	Diameter	10 μm	[27–29]
J_V	Volume change	5%	[27–29]
t_h	Coating thickness	0.2 μm	Assumed
E^{AP}	Young's modulus	130 GPa	[28,29]
ν^{AP}	Poisson's ratio	0.25	[44]
D^{AP}	Li diffusion coefficient	0.025 μm^2/s	[46,47]
$c^{AP}_{100\%}$	Li concentration at 100%	13 fmol/μm^3	[27]
$c^{AP}_{0\%}$	Li concentration at 0%	45.8 fmol/μm^3	[27]
E^C	Young's modulus	22.1 GPa	[48]
ν^C	Poisson's ratio	0.37	[48]
c^C_{res}	Residual Li concentration	43 fmol/μm^3	Assumed
D^C	Li diffusion coefficient	3 μm^2/s	Assumed
E^{CC}	Young's modulus	130 GPa	[47,49]
ν^{CC}	Poisson's ratio	0.25	Assumed
D^{CC}	Li diffusion coefficient	0 μm^2/s	Assumed
E^H	Young's modulus	800 MPa	[36]
ν^H	Poisson's ratio	0.41	[36]
A^H	Eyring's material constant	2×10^{23} s	[36]
τ^H_0	Eyring's material constant	0.7 MPa	[36]
G^H_c	Strain hardening modulus	26.0 MPa	[36]
E^S	Young's modulus	100 MPa	[25]
ν^S	Poisson's ratio	0.24	[50]
A^S	Eyring's material constant	4657 s	Fitted
τ^S_0	Eyring's material constant	0.38 MPa	Fitted
G^S_c	Strain hardening modulus	5.04 MPa	Fitted
D^M	Li diffusion coefficient	3 μm^2/s	[51]
N	Number of inclusions	5	Assumed
D_b	Boundary diffusivity	3 μm^2/s	Assumed
t_0	Maximum interfacial	0.25, 2.5, 40.0 MPa	Assumed
χ_0	Reference opening	0.04 μm	Assumed
D^0_{int}	Initial interfacial diffusivity	0.025 μm/s	Assumed

Fig. 6. The effect of the number of inclusions on stress–strain curves for the BCP system with the soft volume content $f^S_0 = 0.5$.

Fig. 7. Single finite element simulations of the stress–strain curves for the BPC system at different soft-to-hard phase ratios (composite model with five inclusions).

6. Results and discussion

6.1. Elasto-viscoplastic behaviour of the block copolymer matrix

Single-element simulations of block copolymer subject to uniaxial extension were carried to examine (1) the effects of the number of the inclusions, and subsequently (2) the effects of soft-to-hard phase ratio on BCP true stress–strain curves. All simulations were carried at the strain rates of 6.6×10^{-4} s^{-1}. The soft component volume fraction of $f^S_0 = 0.5$ is used, and the average true stress–strain curves out of five simulations for a given number of inclusions are plotted in Fig. 6 with standard error bars. In each simulation, the orientation of the inclusions is chosen randomly. As expected, as the number of the
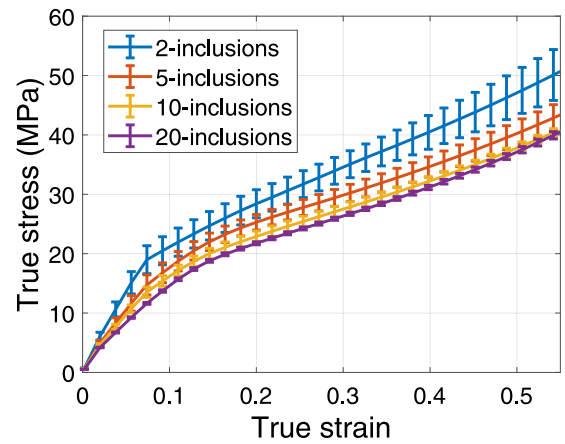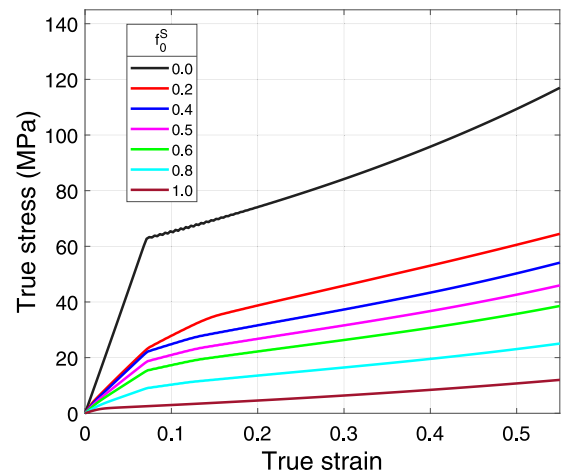
inclusions is increased the error-bars are smaller as the overall inclusion orientation approaches a truly random orientation. There is a price to pay for increased accuracy in terms of the computational time which increases 4-fold for the composite inclusion model with 20 inclusions compared with the model with 5 inclusions. Therefore, for convenience, the composite inclusion model with five inclusions is used to simulate
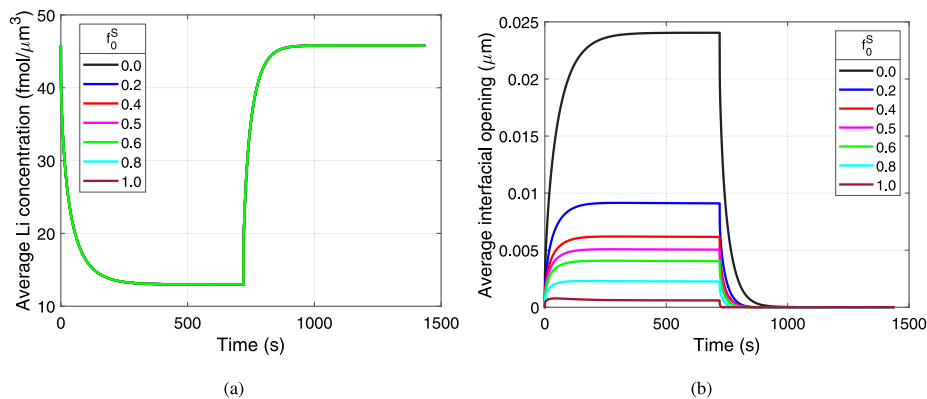
Fig. 8. *Design I*: (a) Average Li concentration for constant interfacial diffusivity D_{int} and (b) Average Interfacial opening displacement; interfacial strength $t_0 = 40$ MPa.
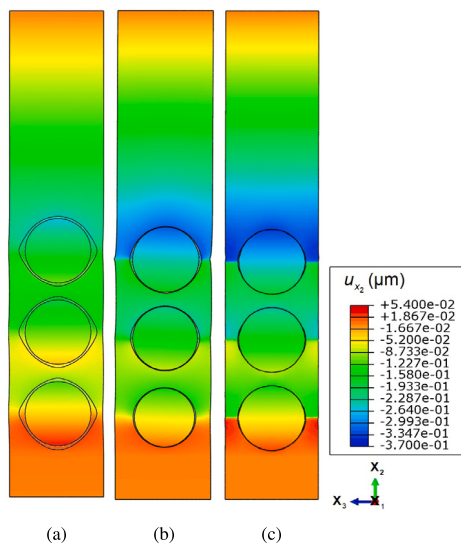

Fig. 9. *Design I*: Vertical displacement at 100% SOC for $t_0 = 40.0$ MPa with (a) $f_0^S = 0.0$ (b) $f_0^S = 0.5$ (c) $f_0^S = 1.0$ under constant diffusivity condition at the interface (displacements are magnified with a scale factor equal to 15).

the mechanical response of the block copolymer within the battery model.

Single-element is simulated with the composite inclusion model (with five inclusions) for different block copolymer volume fractions under uniaxial extension. The stress–strain curves (Fig. 7) show that the system is relaxed quickly from the pure 'hard phase' just with the 0.2 increase in f_0^S, where also a much weaker strain hardening is observed within the simulated range of true strains — this suggests that the soft phase has a strong effect on the mechanical response in this block copolymer model. The change in the behaviour becomes more gradual with the further increase in f_0^S, and it is clearly dominated by the 'soft phase'. These initial findings are expected to impact significantly the response of the battery containing the BCP system.

It is noteworthy to mention that our version of the composite inclusion model for the BCP was verified against the upper bound. Our model's predictions fall within the expected range, as determined by the upper bound. Moreover, our model recovers exactly the elastovis-coplastic response of pure polymer constituents involved in the system, i.e. at $f_0^S = 0.0$ and 1.0.

6.2. Cathode behaviour at the microscale — design case studies

Two design case studies were considered here to investigate the combined effects of the non-linear BCP behaviour and interface strength

on the cathode response. The simulations were carried out for a single charge–discharge cycle, with the half-cycle time interval $t_c = 720$ s (equal for both the charge and discharge process). In particular, the cycle involves de-lithiation of APs (Li diffusing out of the particles), and subsequent volumetric changes (particle shrinkage) during the charge phase. This is then followed by lithiation of APs (Li diffusing into the particles) and thus particle expansion during the discharge phase. Volumetric expansion of APs here is associated with the maximum volumetric change of NMC material equal to 5%

6.2.1. Design case I

6.2.1.1. Effect of the block copolymer material composition. Fig. 8 shows two plots: (1) average Li-ion concentration in APs and (2) average interfacial opening (χ_{Avg}), both as a function of the volume fraction of the soft phase f_0^S. Here, a relatively high interfacial strength was assumed $t_0 = 40$ MPa (for further justification see the subsequent section), and constant (i.e. gap-independent) interfacial diffusivity $D_{\text{int}} = 0.025$ $\mu\text{m}^2/\text{s}$.

The average Li concentration in APs (averaged volumetrically over all three APs) (Fig. 8(a)) decreases rapidly from the initial value of 45.8 fmol/m^3, and then it levels off reaching 13 fmol/m^3. That is then followed by the increase in the average concentration in APs upon the discharge phase. As the interfacial diffusivity is assumed to be constant in this case, all Li can be extracted from the APs during the charge process and thus the average Li concentration in the APs is independent of f_0^S (see Fig. 8(a)).

Then, the plot of the average interfacial gap (averaged over the circumference of every AP, and then over all 3 particles) reflects the above trend and shows initially a rapid increase of the gap (when APs shrink), and then the levelling off as it approaches the end of charge phase — the gap is then reduced upon the discharging phase when APs increase in size, reducing the gap to zero.

The average interfacial opening is found to decrease with the increase in the soft phase. The maximum average opening (corresponding to the end of charge phase, or 100% state of charge (SOC)) of 0.024 μm is found for the BCP with $f_0^S = 0.0$, while it is only 0.0006 μm for $f_0^S = 1.0$. The latter is comparable with the ionic radius of Li, while it is still a little larger than the Li atomic radius (∼0.155 nm) and the expected Li-ion jump (∼0.25 nm [52]). Hence, if the interfacial diffusivity was dependent on the interfacial gap, it could be expected that even such a small interfacial opening predicted here (∼0.6 nm) may form a sufficient barrier to disrupt transport of Li-ions across the AP/BCP interface. Then, the maximum average interfacial opening for other values of f_0^S of 0.2, 0.4, 0.5, 0.6 and 0.8 were found to be 0.0091, 0.0061, 0.005, 0.004 μm and 0.0019 μm, respectively.

To visualize the effect of f_0^S on the shape of the interfacial gap, contour plots of displacements in the vertical direction (x_2) are shown in Fig. 9 at the end of the charge process ($t = 720$ s; 100% SOC). The shape of the gap is found to be the most non-uniform along the
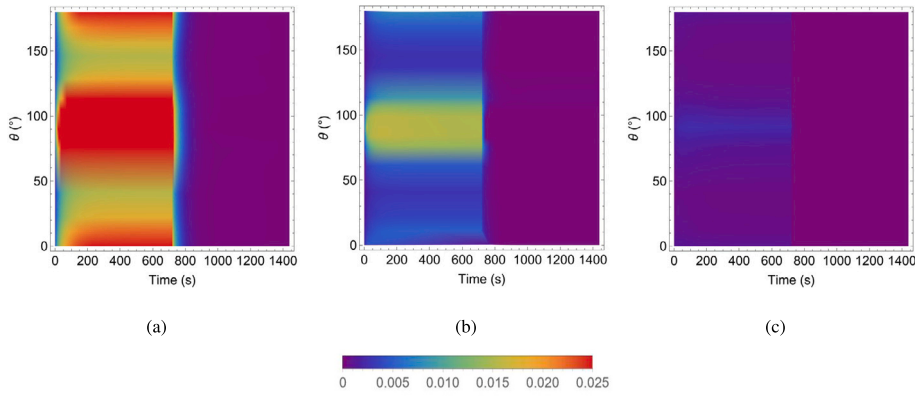
Fig. 10. *Design I*: Angular variation of the interfacial gap [µm] as a function of time for different BCP compositions (a) $f_0^S = 0.0$ (b) $f_0^S = 0.5$ (c) $f_0^S = 1.0$; $t_0 = 40.0$ MPa constant interfacial diffusivity.

interface for f_0^S — that non-uniformity decreases with the increase f_0^S. To investigate it more closely, distribution of the gap along the interface of the middle AP within the angular range from $\theta = 0°$ to $180°$ was plotted as a function of time in Fig. 10. For the system $f_0^S = 0.0$, the largest gap initially appears at θ around $90°$, and then for interface regions around $\theta = 0°$ and $180°$. From around $t = 8$ s the angular extent of those localized domains becomes nearly constant until the end of charging process ($t = 720$ s). For the other two systems $f_0^S = 0.5$ and 1.0, the zone with the largest gap occurs mainly around $\theta = 90°$, with the softest system having the least non-uniform gap distribution. Hence for this cathode design (Design I), the softest BCP matrix would be the most efficient in terms of minimizing interfacial damage, and enabling Li transport paths across the AP/BCP interface.

6.2.1.2. Effect of the interfacial strength. The effect of interfacial strength and its interplay with the non-linear BCP behaviour is described here. The values of strength for the AP/BCP interface were selected in reference to the stress in BCP ($\sigma_{\chi_0}^\alpha$, where $\alpha = H$ or S) at the BCP displacement that corresponds to the displacement (gap) at interface when damage is initiated i.e $\chi = \chi_0$. For that purpose, three different values of interfacial strength were considered to fall into three distinct regimes of BCP behaviour as follows:

$$\begin{cases} t_0 = 0.25 \text{ MPa}: & t_0 < \sigma_{\chi_0}^S < \sigma_{\chi_0}^H \\ t_0 = 2.5 \text{ MPa}: & \sigma_{\chi_0}^S < t_0 < \sigma_{\chi_0}^H \\ t_0 = 40.0 \text{ MPa}: & \sigma_{\chi_0}^H < \sigma_{\chi_0}^S < t_0 \end{cases} \tag{28}$$

where, $\sigma_{\chi_0}^S$ and $\sigma_{\chi_0}^H$ is the uniaxial component of the Cauchy stress in the soft ($f_0^S = 1.0$) and hard ($f_0^S = 0.0$) materials that corresponds to the damage-initiating opening displacement the interface, respectively. For further explanation of how the $\sigma_{\chi_0}^{S,H}$ was calculated see the Appendix.

It is noteworthy to mention that some of the above values of t_0 fall into the range of interfacial strength reported in [12], where the strength of the interface between aluminium and block copolymer (PEO-PC) layers were studied using a macroscopic peel test. The values of interfacial strength reported there vary between 2.625 MPa and 10.25 MPa for BCP ratios f_0^S from 0.74 to 0.3, respectively.

Fig. 11 shows the average interfacial opening as a function of time for different t_0, and f_0^S while constant interfacial diffusivity is assumed 0.025 µm²/s.

In general, it was found that the increase in t_0 reduced the average interfacial gap — however, the level of that reduction depends on f_0^S. Specifically, for $f_0^S = 0.0$ as the interfacial strength increases from 0.25 MPa to 40 MPa, the average gap at the end of the charge process (at $t = 720$ s) is reduced by around 75% from 0.08 to 0.024 µm. Then, for $f_0^S = 1.0$ it is reduced by around 99% from 0.069 µm to 0.0006 µm. For $f_0^S = 0.5$ the average interfacial opening (at $t = 720$ s) is reduced by around 94% from 0.079 µm to 0.005 µm.

Hence, the minimization of the interfacial gap requires both f_0^S and interfacial strength to increase — effectively, a larger interfacial strength (stronger bond) leads to a larger non-linear deformation of the softer BCP material, so the material follows more easily a shrinking AP. However, it is noteworthy to mention that in all the cases studied here the predicted interfacial gap is still larger than a possible jump distance for a Li-ion (~ 0.25 nm) — hence, either an even larger interfacial strength or a much softer BCP may be needed here to reduce the interfacial gap, and allow Li-ions to travel across the interface.

6.2.1.3. Effect of the gap-dependent interfacial diffusivity. Constant interfacial diffusivity was assumed above, whereas in general the transport of Li-ions across the interface can be gap-dependent — thus, the effect of interfacial diffusivity that decreases linearly with the interfacial opening, from $D_{int} = D_{int}^0$ at $\chi = 0$ to $D_{int} = 0$ at $\chi = \chi_0$, was studied here. The intermediate value of the interface strength of $t_0 = 2.5$ MPa was selected here to ensure the corresponding interfacial opening χ_0 can be reached to initiate damage to capture the effects of gap-dependent diffusivity.

Simulation results for the average Li concentration and the corresponding average interfacial gap for different values of f_0^S are shown in Fig. 12. The maximum average opening is in the range from 0.014 to 0.048 µm (see Fig. 12(b)) for three different values of f_0^S, compared with 0.012–0.077 µm for the case with constant diffusivity (see Fig. 11) — hence, the average interfacial opening is reduced for the gap-dependent interfacial diffusivity as less Li-ions can be extracted from the APs during the charging process (see Fig. 11).

However, a somewhat unusual trend for the interfacial gap is found here (Fig. 12) - i.e. despite the average concentration of Li in APs suggesting a reduction in the average gap with the increase of the soft BCP component (f_0^S), the largest average gap was actually predicted at the end of charge for the BCP system with $f_0^S = 0.5$. To investigate this more closely the interfacial gap was extracted at three points (1, 2, and 3) along the interface that corresponded to angular positions of $\theta = 0°$, $45°$ and $90°$, respectively — see Fig. 13. It was found that when $f_0^S = 0.5$, the amplitude of the interfacial gap at the point 3, is excessively high, contributing significantly to the average opening gap (in Fig. 12(b)). However, at the other points, such as 2, the interfacial gap reaches the critical opening $\chi_0 = 0.04$ µm (where the interfacial diffusivity becomes zero) later than in the case with $f_0^S = 0.0$.

It is noteworthy to mention that the average interfacial opening for $f_0^S = 1.0$, after reaching its maximum value at $t = 70.5$ s, slightly decreases as a result of mechanical (stress) relaxation due to the viscous nature of polymers (captured here by our elastoviscoplastic constitutive model) that increases with f_0^S i.e. it is the largest for the softest polymer, $f_0^S = 1.0$. Hence, in the context of Design 1, where a greater amount of polymer is incorporated into the system, this effect becomes more pronounced and readily apparent. This mechanical relaxation can
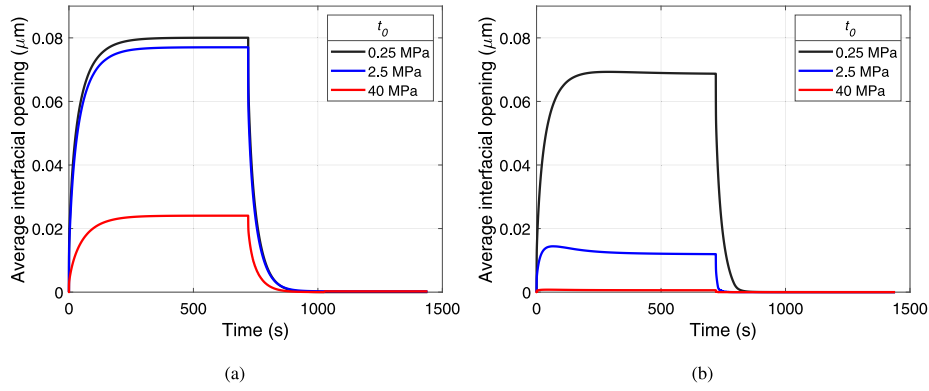
ARTICLE IN PRESS

S. Bazazzadeh et al.   International Journal of Mechanical Sciences xxx (xxxx) xxx

Fig. 11. *Design I*: Variation of the average interfacial opening displacement in time for different BCP compositions (a) $f_0^S = 0.0$ (b) $f_0^S = 1.0$; constant interfacial diffusivity.
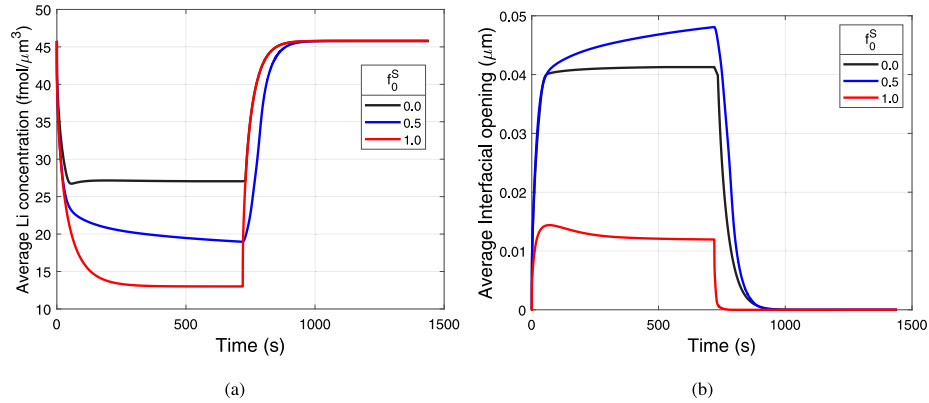

Fig. 12. *Design I*: (a) Average Li concentration with $t_0 = 2.5$ MPa and (b) Average Interfacial opening displacement under linear interface diffusivity condition at the interface.

manifest as changes in shape, stress distribution, or other mechanical properties over time, which are additional considerations in the design and performance of ASSBs based on polymer-based systems.

To visualize it further, contour plots of the interfacial diffusivity along the interface of the middle AP from $\theta = 0°$ to $180°$ are shown as a function of time in Fig. 14. The diffusivity for nearly a full range of θ goes quickly to zero just after $t = 45$ s when $f_0^S = 0.0$ (see Fig. 14(a)). However, for $f_0^S = 0.5$, the diffusivity remains non-zero around $\theta \simeq 45°$ and $\theta \simeq 135°$ for longer and then becomes zero (see Fig. 14(b)). For $f_0^S = 1.0$ the diffusivity across the interface remains non-zero throughout the entire charging process except for the region around $\theta \simeq 90°$ (see Fig. 14(c)) where no transfer of Li takes place. In addition, the ratio of the interfacial region with non-zero diffusivity to the total interface domain was found to be 76%, 68%, and 0% for $f_0^S = 0.0$, 0.5, and 1.0, respectively, at time of $t = 186$ s (i.e. when the interfacial diffusivity at point 2 has already reached zero for the hard material). Thus, the average amount of lithium extracted from the AP is higher for $f_0^S = 0.5$ compared with $f_0^S = 0.0$.

It is important to highlight that it is not straightforward rule stating that the gap size for the block copolymer with $f_0^S = 0.5$ should be smaller than that for $f_0^S = 0.0$. This is because the magnitude of the gap depends on the combined effect of block copolymer composition/response and non-constant (gap-dependent interfacial diffusivity). This combination results in different shapes of the gap around the circumference of active particles (APs). For $f_0^S = 0.0$, the gap is uniform around the circumference. However, when $f_0^S = 0.5$, the gap becomes uneven around the circumference, with the largest opening at the poles of the AP — this stems from a larger deformation of a softer BCP and reduction of Li-ion transport across the interface due to gap-dependent interfacial diffusivity. This larger opening at the poles has a more significant effect on the average gap size than other regions around the AP.
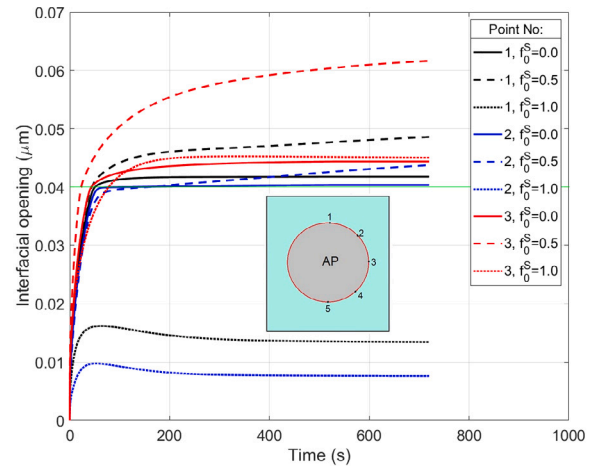

Fig. 13. *Design I*: Interfacial opening displacement for point 1,2, and 3 with $t_0 = 2.5$ MPa under linear interface diffusivity.

6.2.2. Design case II

6.2.2.1. Effect of the BCP material composition of the coating.
The effects of the soft-to-hard phase ratio f_0^S in the BCP coating on the average concentration and average interfacial opening were studied for the interfacial strength of $t_0 = 40$ MPa and constant interfacial diffusivity ($D_{int} = 0.025$). Only the charge process was considered here.

The average Li concentration in the APs is found to be the same across different f_0^S (see Fig. 15(a)). Similarly to *Design I*, an increase in f_0^S leads to a reduction in the opening — however, the level of that reduction is smaller here than for the *Design I*. In particular, the
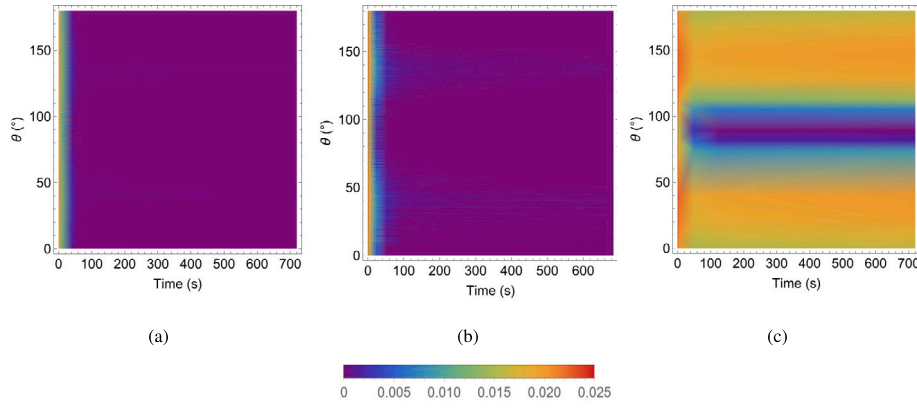
Fig. 14. *Design I*: Angular variation of the diffusivity [μm²/s] as a function of time for different BCP compositions (a) $f_0^S = 0.0$ (b) $f_0^S = 0.5$ (c) $f_0^S = 1.0$; $t_0 = 40.0$ MPa linear interfacial diffusivity.
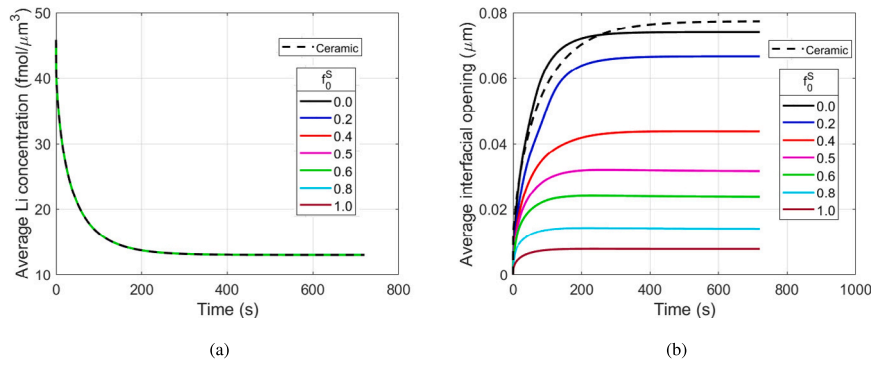

Fig. 15. *Design II*: (a) Average Li concentration for constant interfacial diffusivity D_{int} and (b) Average Interfacial opening displacement; interfacial strength $t_0 = 40$ MPa.

maximum average opening at the end of charge decreases by an order of magnitude from 0.074 μm for $f_0^S = 0.0$ to 0.0078 μm at $f_0^S = 1.0$.

Average opening of *Design II* is also compared with a conventional system composed of APs fully embedded within a ceramic argyrodite matrix (Li_6PS_5Cl) (i.e. case without the coating). The maximum average gap (end of charge) for the ceramic system is predicted to be 0.0774 μm, which is close to the case with the hard polymer coating ($f_0^S = 0.0$), with the difference between the two of around 4.4%.

Hence under the imposed assumptions and from the mechanical point of view, it is concluded that the application of the BCP coating with a considerable amount of soft phase can significantly contribute to the damage reduction at the AP/coating interface.

6.2.2.2. Effect of the interfacial strength. The average interfacial gap was found to decrease with the increased interfacial strength t_0 from 0.25 MPa to 40 MPa (Fig. 16). However, that decrease was found to be dependent on the BCP material composition. Specifically, for the coating made of the hardest BCP ($f_0^S = 0.0$), the average gap is only slightly reduced from 0.08 to 0.074 μm (reduction of $\sim$ 8%) for $t_0 = 0.25$ MPa and 40 MPa, respectively. In contrast, the BCP system with the softest coating experiences a substantial reduction in the average gap, by an order of magnitude, from 0.08 to 0.0078 μm ($\sim$ 90%). For completeness, a reduction in the average interfacial gap from 0.08 to 0.031 μm ($\sim$ 61%) was found for the BCP system with $f_0^S = 0.5$. The above clearly demonstrates that the most effective way of reducing interfacial damage is by combining sufficiently large interface strength and BCP with a considerable amount of soft component.

6.2.2.3. Effect of the gap-dependent interfacial diffusivity. The system with the softest coating allows for more Li to be extracted from the APs as indicated by the average Li concentration in APs at the end of charge — this results in a slightly greater particle contraction (Fig. 17(a)),

similarly to *Design I* (Section 6.2.1.3). All that results from the non-uniform distribution of the interfacial gap along the interface, namely: (1) the Li extraction is allowed to take place across those local interfacial domains where the gap is below a critical value at which the interfacial diffusivity is zero, while (2) the value of average interfacial opening is dictated by those local domains along the interface where the opening is significant but occurring over a small interfacial domain. As a result, the average interfacial opening in the softer system is found to be slightly larger than in the stiffer BCP system. The range of maximum average opening is between 0.04 and 0.042 μm for f_0^S from 0.0 to 1.0 (Fig. 17(b)). In comparison, the constant diffusivity case yields a maximum average opening from 0.074 to 0.079 μm, as shown in Fig. 16.

6.3. Sensitivity analysis of the average interfacial opening (Designs I and II)

To compare the effect of different design parameters on the average interfacial opening and determine most influential parameters, the relative sensitivity gradients [14] were determined with respect to three design parameters P, namely the coating thickness, volume fraction f_0^S, and interfacial strength. Specifically, the relative sensitivity of the average opening denoted as χ_{Avg} (design function) with respect to the design parameter P is given by:

$$S(P) = \frac{\partial \chi_{Avg}}{\partial P} \frac{P}{\chi_{Avg}}, \quad \text{where} \quad \frac{\partial \chi_{Avg}}{\partial P} \cong \frac{\Delta \chi_{Avg}}{\Delta P}$$
$$= \frac{\chi_{Avg}(P + \Delta P) - \chi_{Avg}(P)}{\Delta P} \tag{29}$$

where P was taken as the nominal (initial) value of each design parameter, i.e. $t_h = 0.2$ μm, $f_0^S = 0.5$ and $t_0 = 40$ MPa. A small perturbation
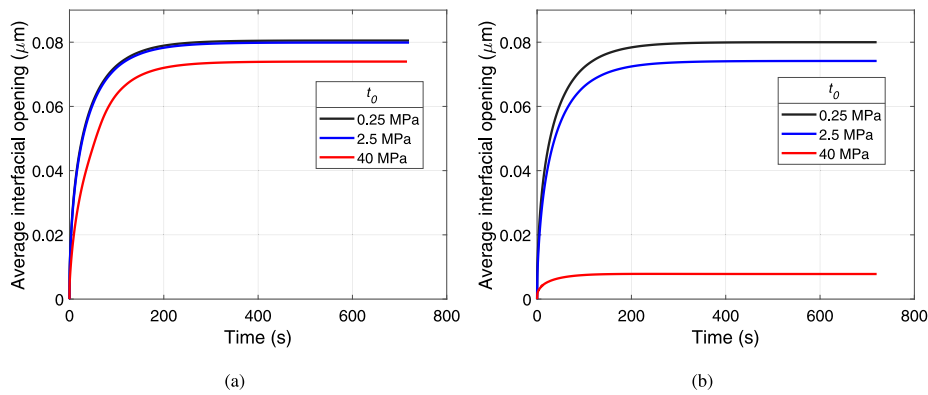
Fig. 16. *Design II*: Variation of the average interfacial opening displacement in time for different BCP compositions (a) $f_0^S = 0.0$ (b) $f_0^S = 1.0$; constant interfacial diffusivity.
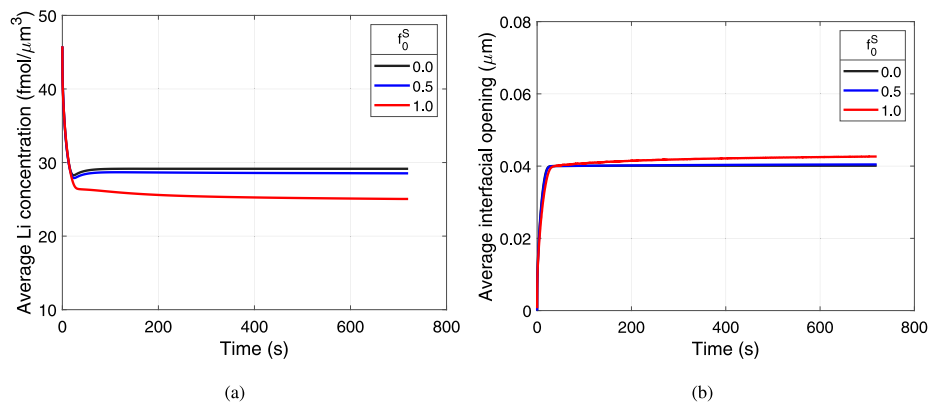

Fig. 17. *Design II*: (a) Average Li concentration with $t_0 = 2.5$ MPa and (b) Average Interfacial opening displacement under linear interface diffusivity condition at the interface.
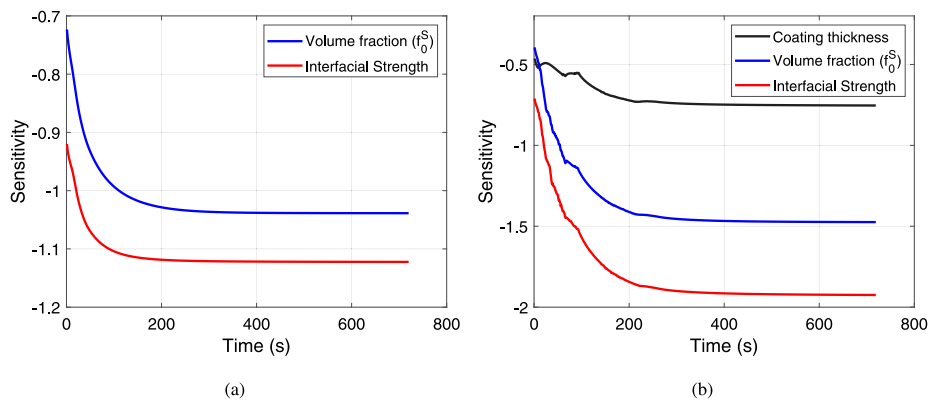

Fig. 18. Evolution of sensitivity gradients of the average interfacial gap for (a) *Design I* and (b) *Design II*.

of 1% of the nominal parameter value was used to evaluate ΔP. The results of the sensitivity study are plotted in Fig. 18 as a function of time (until the end of charge phase) for *Designs I* and *II*. For both designs, all the sensitivity gradients are negative throughout the entire charge process, which suggests that the design function (average opening) is reduced with the increase in design parameter. In both case studies, the sensitivity results predict the interfacial strength as the most significant design parameter here (given the largest absolute value of the relative sensitivity gradient) over the course of the entire charging phase. The volume fraction f_0^S is the least influential parameter among the parameters studied for *Design I*, while the coating thickness is the least effective parameter among the parameters studied in *Design II* – only at the very start of the process ($t < 12$ s), f_0^S is to have the least influence –

here the effect of the coating thickness is around 14% more influential than the volume fraction at the beginning of the charging process.

7. Conclusions

This paper provided a new insight into the role of model block copolymer (BCPs) systems in minimizing the interfacial damage in ASSB cathodes. Two cathode design concepts with BCPs were investigated computationally, i.e. (1) *Design I* where the cathode APs were embedded in a continuous phase of a BCP matrix with the varying soft-to-hard phase ratio, and (2) *Design II* where the cathode APs were coated with a thin layer of the BCP material (again with

different soft-to-hard phase ratios) and embedded in a ceramic electrolyte. For that, a computational micromechanics approach was developed within a non-linear diffusion-mechanics framework that combined a finite-strain elasto-viscoplastic constitutive model for the BCP, traction–separation law for the cathode active particle (AP)/BCP interface, pressure-dependent Li transport and damage-dependent diffusivity. The approach was implemented numerically using a non-linear finite element solver and accompanied by a simple sensitivity analysis.

The ability of the BCP to accommodate volumetric changes of the APs and minimizing their interface debonding from the BCP matrix/coating was investigated computationally throughout the charge–discharge process by using the proposed approach and a simplified 3D geometrical representation of the cathode microstructure. The simulation results showed that the interfacial opening (gap) and its shape are strongly dependent on the chosen combination of the BCP material composition (i.e. amount of the soft phase) and the interfacial strength between the APs and the surrounding matrix. Different combinations of those parameters showed that when the interface strength was chosen to be below the stress in BCP (that corresponds to the displacement initiating damage at the interface), the interfacial opening was found to be more uniform around all the circumference of the APs, and the volume fraction of the soft phase has little influence on the opening. However, when the interfacial strength was between the stress for the hard and soft BCP, the interfacial gap and its shape were significantly affected by the amount of soft phase in the BCP. As the material surrounding the APs became softer the shape of the gap changed from the uniform (around the entire particle circumference) to the non-uniform with the maximum values gap occurring at the poles of the APs. Subsequently, when the interfacial strength exceeded the aforementioned stress value in the hard BCP, the interfacial gap was reduced significantly and the maximum values gap occurred at the poles of the APs.

Furthermore, the results showed that when the interfacial diffusivity was assumed to be gap-dependent (i.e. linearly decaying with the increase in gap), the interfacial gap was reduced both in both design case studies when the BCP was predominantly made of the hard phase. Finally, a simple sensitivity analysis of the interfacial gap to the studied design parameters, revealed that the interfacial strength would play the most vital role in minimizing interfacial damage. On the other hand, the coating thickness was found to have the least influence on reducing the interfacial damage over the majority of the charge phase.

In summary, our model offers fresh insights into combined effects of BCP elastoviscoplastic behaviour and interfacial characteristic on an in-situ diffusion-mechanics behaviour of polymer-based ASSB cathodes that entails certain simplifications of ASSB cathode microstructure. Future work should account for more realistic representations of cathode microstructure (e.g., non-spherical particle shape) to understand its effects on Li-ion transport and stress fields.

CRediT authorship contribution statement

Soheil Bazazzadeh: Methodology, Software, Investigation, Visualization, Formal analysis, Writing – original draft. **Mauro Pasta:** Conceptualization, Project administration, Funding acquisition, Writing review & editing. **Łukasz Figiel:** Conceptualization, Methodology, Supervision, Project administration, Funding acquisition, Formal analysis, Writing – review & editing.

Declaration of competing interest

The authors declare the following financial interests/personal relationships which may be considered as potential competing interests: Soheil Bazazzadeh reports financial support was provided by The Faraday Institution.

Data availability

Data will be made available on request.

Appendix. Interfacial strength values — further information

Selection of the interfacial strength t_0 was discussed in Sections Section 6.2.1.2. As mentioned there, three regimes of block copolymer
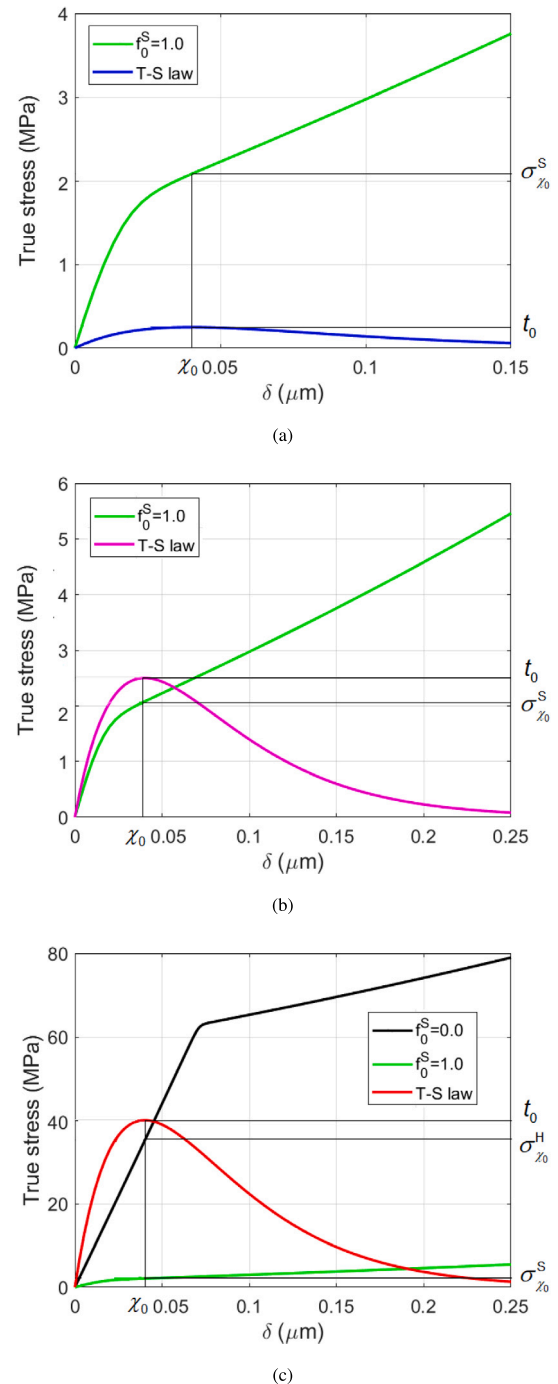

(a)

(b)

(c)

Fig. A.19. Determination of interfacial strength: uniaxial stress–displacement and traction–separation (T–S) curves for different regimes (a) $t_0 < \sigma_{\chi_0}^S < \sigma_{\chi_0}^H$ (b) $\sigma_{\chi_0}^S < t_0 < \sigma_{\chi_0}^H$ (c) $\sigma_{\chi_0}^H < \sigma_{\chi_0}^S < t_0$.

(BCP) behaviour were considered when selecting values of the interfacial strength in this work. The point of reference are the stress values $\sigma^{\alpha}_{\chi_0}$ (where α = H or S) corresponding to the displacements equivalent (in value) to the interfacial opening at damage initiation χ_0.

To determine $\sigma^{\alpha}_{\chi_0}$, single-element simulations were carried out under uniaxial extension to determine the stress–displacement curves as shown in Fig. A.19 for BCPs with soft and hard components. They were then compared with relevant traction–separation plots to choose three different values of interface strength $t_0 = 0.25$, 2.5 and 40 MPa, that fall into three different regimes of BCP behaviour as described by Eq. (28) in 6.2.1.2.

References

[1] Armand M, Tarascon JM. Building better batteries. Nature 2008;451(7179):652–7. http://dx.doi.org/10.1038/451652a.

[2] Scrosati B, Hassoun J, Sun Y-K. Lithium-ion batteries. A look into the future. Energy Environ Sci 2011;4(9):3287–95. http://dx.doi.org/10.1039/C1EE01388B.

[3] Stallard JC, Wheatcroft L, Booth SG, Boston R, Corr SA, De Volder MFL, Inkson BJ, Fleck NA. Mechanical properties of cathode materials for lithium-ion batteries. Joule 2022;6(5):984–1007. http://dx.doi.org/10.1016/j.joule.2022.04.001, URL https://www.sciencedirect.com/science/article/pii/S2542435122001398.

[4] Janek J, Zeier WG. A solid future for battery development. Nat Energy 2016;1(9):16141. http://dx.doi.org/10.1038/nenergy.2016.141.

[5] Kasemchainan J, Bruce P. All-solid-state batteries and their remaining challenges. Johns Matthey Technol Rev 2018;62(2):177–80.

[6] Kim JG, Son B, Mukherjee S, Schuppert N, Bates A, Kwon O, Choi MJ, Chung HY, Park S. A review of lithium and non-lithium based solid state batteries. J Power Sources 2015;282:299–322. http://dx.doi.org/10.1016/j.jpowsour.2015.02.054, URL https://www.sciencedirect.com/science/article/pii/S0378775315002773.

[7] Ma J, Chen B, Wang L, Cui G. Progress and prospect on failure mechanisms of solid-state lithium batteries. J Power Sources 2018;392:94–115. http://dx.doi.org/10.1016/j.jpowsour.2018.04.055, URL https://www.sciencedirect.com/science/article/pii/S0378775318303987.

[8] Xu L, Tang S, Cheng Y, Wang K, Liang J, Liu C, Cao Y-C, Wei F, Mai L. Interfaces in Solid-State Lithium Batteries. Joule 2018;2(10):1991–2015. http://dx.doi.org/10.1016/j.joule.2018.07.009.

[9] Zhang F, Huang Q-A, Tang Z, Li A, Shao Q, Zhang L, Li X, Zhang J. A review of mechanics-related material damages in all-solid-state batteries: Mechanisms, performance impacts and mitigation strategies. Nano Energy 2020;70:104545. http://dx.doi.org/10.1016/j.nanoen.2020.104545, URL https://www.sciencedirect.com/science/article/pii/S2211285520301026.

[10] Feng J, Wang L, Chen Y, Wang P, Zhang H, He X. PEO based polymer-ceramic hybrid solid electrolytes: a review. Nano Convergence 2021;8(1):2. http://dx.doi.org/10.1186/s40580-020-00252-5.

[11] Yang H, Wu N. Ionic conductivity and ion transport mechanisms of solid-state lithium-ion battery electrolytes: A review. Energy Sci Eng 2022;10(5):1643–71. http://dx.doi.org/10.1002/ese3.1163.

[12] Gregory GL, Gao H, Liu B, Gao X, Rees GJ, Pasta M, Bruce PG, Williams CK. Buffering volume change in solid-state battery composite cathodes with CO2-derived block polycarbonate ethers. J Am Chem Soc 2022;144(38):17477–86. http://dx.doi.org/10.1021/jacs.2c06138.

[13] Hou X, Siow KS. Mechanical properties and ionic conductivities of plasticized polymer electrolytes based on ABS/PMMA blends. Polymer 2000;41(24):8689–96. http://dx.doi.org/10.1016/S0032-3861(00)00270-6, URL https://www.sciencedirect.com/science/article/pii/S0032386100002706.

[14] Lippmann P, Poluektov M, Figiel Ł. Stress-affected lithiation reactions in elasto-viscoplastic Si particles with hyperelastic polymer coatings: A nonlinear chemo-mechanical finite-element study. 2018, http://dx.doi.org/10.3390/coatings8120455.

[15] Wu H, Yu G, Pan L, Liu N, McDowell MT, Bao Z, Cui Y. Stable Li-ion battery anodes by in-situ polymerization of conducting hydrogel to conformally coat silicon nanoparticles. Nature Commun 2013;4(1):1943. http://dx.doi.org/10.1038/ncomms2941.

[16] Klinsmann M, Rosato D, Kamlah M, McMeeking RM. Modeling crack growth during Li insertion in storage particles using a fracture phase field approach. J Mech Phys Solids 2016;92:313–44. http://dx.doi.org/10.1016/j.jmps.2016.04.004, URL https://www.sciencedirect.com/science/article/pii/S0022509616300965.

[17] Zhu X, Chen Y, Chen H, Luan W. The diffusion induced stress and cracking behaviour of primary particle for Li-ion battery electrode. Int J Mech Sci 2020;178:105608. http://dx.doi.org/10.1016/j.ijmecsci.2020.105608, URL https://www.sciencedirect.com/science/article/pii/S0020740319340354.

[18] Zhang X, Chen H, Fang D. Effects of surface stress on lithium-ion diffusion kinetics in nanosphere electrodes of lithium-ion batteries. Int J Mech Sci 2020;169:105323. http://dx.doi.org/10.1016/j.ijmecsci.2019.105323, URL https://www.sciencedirect.com/science/article/pii/S0020740319334502.

[19] Bucci G, Talamini B, Renuka Balakrishna A, Chiang Y-M, Carter WC. Mechanical instability of electrode-electrolyte interfaces in solid-state batteries. Phys Rev Mater 2018;2(10):105407. http://dx.doi.org/10.1103/PhysRevMaterials.2.105407, URL https://link.aps.org/doi/10.1103/PhysRevMaterials.2.105407.

[20] Dimitrijevic BJ, Aifantis KE, Hackl K. The influence of particle size and spacing on the fragmentation of nanocomposite anodes for Li batteries. J Power Sources 2012;206:343–8. http://dx.doi.org/10.1016/j.jpowsour.2012.01.065, URL https://www.sciencedirect.com/science/article/pii/S0378775312001644.

[21] Zhao Y, Wang R, Martínez-Pañeda E. A phase field electro-chemo-mechanical formulation for predicting void evolution at the Li–electrolyte interface in all-solid-state batteries. J Mech Phys Solids 2022;167:104999. http://dx.doi.org/10.1016/j.jmps.2022.104999, URL https://www.sciencedirect.com/science/article/pii/S0022509622001879.

[22] Grazioli D, Verners O, Zadin V, Brandell D, Simone A. Electrochemical-mechanical modeling of solid polymer electrolytes: Impact of mechanical stresses on Li-ion battery performance. Electrochim Acta 2019;296:1122–41. http://dx.doi.org/10.1016/j.electacta.2018.07.234, URL https://www.sciencedirect.com/science/article/pii/S0013468618317626.

[23] Bucci G, Swamy T, Chiang Y-M, Carter WC. Modeling of internal mechanical failure of all-solid-state batteries during electrochemical cycling, and implications for battery design. J Mater Chem A 2017;5(36):19422–30. http://dx.doi.org/10.1039/C7TA03199H.

[24] Yu H-C, Taha D, Thompson T, Taylor NJ, Drews A, Sakamoto J, Thornton K. Deformation and stresses in solid-state composite battery cathodes. J Power Sources 2019;440:227116. http://dx.doi.org/10.1016/j.jpowsour.2019.227116, URL https://www.sciencedirect.com/science/article/pii/S0378775319311097.

[25] Sultanova L, Figiel Ł. Microscale diffusion-mechanics model for a polymer-based solid-state battery cathode. Comput Mater Sci 2021;186:109990. http://dx.doi.org/10.1016/j.commatsci.2020.109990, URL https://www.sciencedirect.com/science/article/pii/S092702562030481X.

[26] van Dommelen JAW, Parks DM, Boyce MC, Brekelmans WAM, Baaijens FPT. Micromechanical modeling of the elasto-viscoplastic behavior of semi-crystalline polymers. J Mech Phys Solids 2003;51(3):519–41. http://dx.doi.org/10.1016/S0022-5096(02)00063-7, URL https://www.sciencedirect.com/science/article/pii/S0022509602000637.

[27] Chen C-H, Brosa Planella F, O'Regan K, Gastol D, Widanage WD, Kendrick E. Development of experimental techniques for parameterization of multi-scale lithium-ion battery models. J Electrochem Soc 2020;167(8):080534. http://dx.doi.org/10.1149/1945-7111/ab9050.

[28] de Vasconcelos LS, Xu R, Li J, Zhao K. Grid indentation analysis of mechanical properties of composite electrodes in Li-ion batteries. Extreme Mech Lett 2016;9:495–502.

[29] Xu R, Sun H, de Vasconcelos LS, Zhao K. Mechanical and structural degradation of LiNixMnyCozO2 cathode in Li-Ion batteries: An experimental study. J Electrochem Soc 2017;164(13):A3333. http://dx.doi.org/10.1149/2.1751713jes.

[30] Dudney NJ, Bates JB, Neudecker BJ. Thin-film materials for solid-state rechargeable batteries. Oxford: Elsevier; 2001, p. 9302–6. http://dx.doi.org/10.1016/B0-08-043152-6/01677-6, URL https://www.sciencedirect.com/science/article/pii/B0080431526016776.

[31] Kanamura K. Secondary batteries – lithium rechargeable systems | negative electrodes: Lithium metal. Amsterdam: Elsevier; 2009, p. 27–39. http://dx.doi.org/10.1016/B978-044452745-5.00191-X, URL https://www.sciencedirect.com/science/article/pii/B978044452745500191X.

[32] Bates FS, Fredrickson GH. Block copolymers—Designer soft materials. Phys Today 1999;52(2):32–8. http://dx.doi.org/10.1063/1.882522.

[33] Parks DM, Ahzi S. Polycrystalline plastic deformation and texture evolution for crystals lacking five independent slip systems. J Mech Phys Solids 1990;38(5):701–24. http://dx.doi.org/10.1016/0022-5096(90)90029-4, URL https://www.sciencedirect.com/science/article/pii/0022509690900294.

[34] Lee BJ, Ahzi S, Asaro RJ. On the plasticity of low symmetry crystals lacking five independent slip systems. Mech Mater 1995;20(1):1–8. http://dx.doi.org/10.1016/0167-6636(94)00045-I, URL https://www.sciencedirect.com/science/article/pii/016766369400045I.

[35] Buckley CP, Jones DC. Glass-rubber constitutive model for amorphous polymers near the glass transition. Polymer 1995;36(17):3301–12. http://dx.doi.org/10.1016/0032-3861(95)99429-X, URL https://www.sciencedirect.com/science/article/pii/003238619599429X.

[36] Klompen ETJ, Engels TAP, Govaert LE, Meijer HEH. Modeling of the postyield response of glassy polymers: Influence of thermomechanical history. Macromolecules 2005;38(16):6997–7008. http://dx.doi.org/10.1021/ma050498v.

[37] Tervoort TA, Smit RJM, Brekelmans WAM, Govaert LE. A constitutive equation for the elasto-viscoplastic deformation of glassy polymers. Mech Time-Dependent Mater 1997;1(3):269–91. http://dx.doi.org/10.1023/A:1009720708029.

[38] Zhang X, Shyy W, Marie Sastry A. Numerical simulation of intercalation-induced stress in Li-Ion battery electrode particles. J Electrochem Soc 2007;154(10):A910. http://dx.doi.org/10.1149/1.2759840.

[39] Rose JH, Ferrante J, Smith JR. Universal binding energy curves for metals and bimetallic interfaces. Phys Rev Lett 1981;47(9):675–8. http://dx.doi.org/10.1103/PhysRevLett.47.675, URL https://link.aps.org/doi/10.1103/PhysRevLett.47.675, PRL.

[40] Gupta H, Singh SK, Singh VK, Tripathi AK, Srivastava N, Tiwari RK, Mishra R, Meghnani D, Singh RK. Development of polymer electrolyte and cathode material for Li-batteries. J Electrochem Soc 2019;166(3):A5187. http://dx.doi.org/10.1149/2.0331903jes.

[41] Weber R, Fell CR, Dahn JR, Hy S. Operando X-ray diffraction study of polycrystalline and single-crystal LixNi0.5Mn0.3Co0.2o2. J Electrochem Soc 2017;164(13):A2992. http://dx.doi.org/10.1149/2.0441713jes.

[42] Wang Z, Yang L, Zhu S, Song W-L, Chen H-S. Exploring mechanical failure of porous electrode meso structure using the discrete element method. Extreme Mech Lett 2021;46:101252. http://dx.doi.org/10.1016/j.eml.2021.101252, URL https://www.sciencedirect.com/science/article/pii/S2352431621000511.

[43] Zhu J, Li W, Xia Y, Sahraei E. Testing and modeling the mechanical properties of the granular materials of graphite anode. J Electrochem Soc 2018;165(5):A1160. http://dx.doi.org/10.1149/2.0141807jes.

[44] Cheng EJ, Hong K, Taylor NJ, Choe H, Wolfenstine J, Sakamoto J. Mechanical and physical properties of LiNi0.33Mn0.33Co0.33O2 (NMC). J Eur Ceram Soc 2017;37(9):3213–7. http://dx.doi.org/10.1016/j.jeurceramsoc.2017.03.048, URL https://www.sciencedirect.com/science/article/pii/S0955221917301966.

[45] Amin R, Chiang Y-M. Characterization of electronic and ionic transport in Li1-xNi0.33Mn0.33Co0.33O2 (NMC333) and Li1-xNi0.50Mn0.20Co0.30O2 (NMC523) as a function of Li content. J Electrochem Soc 2016;163(8):A1512. http://dx.doi.org/10.1149/2.0131608jes.

[46] Capron O, Gopalakrishnan R, Jaguemont J, Van Den Bossche P, Omar N, Van Mierlo J. On the ageing of high energy lithium-ion batteries—Comprehensive electrochemical diffusivity studies of harvested nickel manganese cobalt electrodes. 2018, http://dx.doi.org/10.3390/ma11020176.

[47] Lee Y-G, Fujiki S, Jung C, Suzuki N, Yashiro N, Omoda R, Ko D-S, Shiratsuchi T, Sugimoto T, Ryu S, Ku JH, Watanabe T, Park Y, Aihara Y, Im D, Han IT. High-energy long-cycling all-solid-state lithium metal batteries enabled by silver–carbon composite anodes. Nat Energy 2020;5(4):299–308. http://dx.doi.org/10.1038/s41560-020-0575-z.

[48] Deng Z, Wang Z, Chu I-H, Luo J, Ong SP. Elastic properties of alkali superionic conductor electrolytes from first principles calculations. J Electrochem Soc 2016;163(2):A67. http://dx.doi.org/10.1149/2.0061602jes.

[49] Zhang G, Zhou W, Chen M, Wang Q, Li A, Xu J, Chen J. Stainless steel foil: A more appropriate current collector than titanium foil for the cathodes of aqueous zinc ion batteries. Electrochim Acta 2023;437:141519. http://dx.doi.org/10.1016/j.electacta.2022.141519, URL https://www.sciencedirect.com/science/article/pii/S0013468622016760.

[50] Kelly T, Ghadi BM, Berg S, Ardebili H. In situ study of strain-dependent ion conductivity of stretchable polyethylene oxide electrolyte. Sci Rep 2016;6. http://dx.doi.org/10.1038/srep20128, URL https://www.scopus.com/inward/record.uri?eid=2-s2.0-84957600678&doi=10.1038%2fsrep20128&partnerID=40&md5=ec9afd617f381bf6f593bb6167221b32, Export Date: 20 October 2022; Cited By: 46.

[51] Karo J, Brandell D. A molecular dynamics study of the influence of side-chain length and spacing on lithium mobility in non-crystalline LiPF6·PEOx; x=10 and 30. Solid State Ion 2009;180(23):1272–84. http://dx.doi.org/10.1016/j.ssi.2009.07.009, URL https://www.sciencedirect.com/science/article/pii/S0167273809002793.

[52] Hiebl C, Loch P, Brinek M, Gombotz M, Gadermaier B, Heitjans P, Breu J, Wilkening HMR. Rapid low-dimensional Li(+) ion hopping processes in synthetic hectorite-type Li(0.5)[Mg(2.5)Li(0.5)]Si(4)O(10)F(2). Chem Mater 2020;32(17):7445–57. http://dx.doi.org/10.1021/acs.chemmater.0c02460.